

# Performance of the MICE diagnostic systems

5

The MICE Collaboration

## Abstract

Muon beams of low emittance provide the basis for the intense, well characterised neutrino beams of a neutrino factory and for multi-TeV lepton-antilepton collisions at a muon collider. The international Muon Ionization Cooling Experiment (MICE) has demonstrated ionization cooling, the technique by which it is proposed to reduce the phase-space volume occupied by the muon beam. This paper will describe the detectors used in the experiment, their performances and how they have been used as a full comprehensive diagnostic system, including the liquid hydrogen absorber installed for the emittance reduction measurements.

## Contents

15	<b>1 Introduction</b>	2
	<b>2 Time-of-Flight Detectors</b>	2
	2.1 Introduction . . . . .	2
	2.2 Performance . . . . .	4
20	<b>3 Cherenkov Detectors</b>	5
	3.1 Introduction . . . . .	5
	3.2 Performance . . . . .	6
	<b>4 KLOE-Light Calorimeter</b>	8
	4.1 Introduction . . . . .	8
	4.2 Performance . . . . .	8
25	<b>5 Electron Muon Ranger</b>	11
	5.1 Introduction . . . . .	11
	5.2 Performance . . . . .	12
30	<b>6 Trackers</b>	15
	6.1 Introduction . . . . .	15
	6.2 Performance and Reconstruction . . . . .	16
	6.3 Efficiency evolution . . . . .	18
	<b>7 Global Track Matching reconstruction</b>	18
35	<b>8 Beam-based detector alignment</b>	19
	8.1 Introduction . . . . .	19
	8.2 Analysis method . . . . .	20
	<b>9 Liquid Hydrogen absorber</b>	23
	9.1 Introduction . . . . .	23
	9.2 Systematic studies . . . . .	24

40 **1 Introduction**

To include:

- Motivation
- Outline of the experiment

**2 Time-of-Flight Detectors**45 **2.1 Introduction**

Three time-of-flight detectors (TOF0, TOF1, TOF2) were built and installed at RAL in 2008 and 2009 to measure the position and the time of crossing particles. TOF0 and TOF1 [1], [2], [3] were placed upstream of the cooling channel, and TOF2 [4] was downstream of the channel, mounted in front of the KL, as shown in Fig. 1. The time of flight between two TOF stations provides particle identification information and can also 50 be used for momentum measurement. TOF1 served most of the time also as an experimental trigger. They operated smoothly during the so-called Step I and Step IV [5], [6] running periods of the MICE experiment and were essential for all the measurements done.

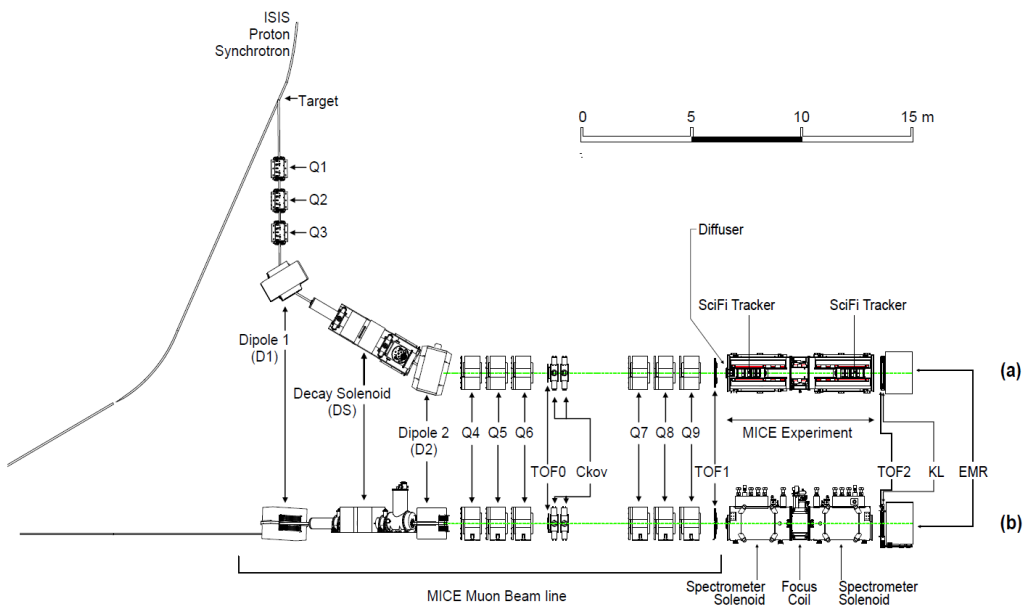


Figure 1: MICE experiment in the Step IV configuration, showing the full beam line and cooling channel elements with all the detectors.

The good performances of the TOF detectors, over an extended period of time, enabled the MICE experiment to characterize fully its muon beams during Step I data-taking, by measuring their emittance [7] and assessing 55 their pion contamination [8].

Each TOF station was made of two planes of fast 1" thick scintillator bars oriented along X and Y directions, respectively. The bars were made of BC404 plastic scintillator<sup>1</sup>. A simple fishtail light-guide was used to

---

<sup>1</sup>Emission maximum at 408 nm, decay time 1.8 ns, attenuation length 160 cm

attach each end of a bar to R4998 Hamamatsu fast photomultiplier tubes<sup>2</sup>. R4998 PMTs were delivered by Hamamatsu in assemblies (H6533MOD) that included the PMT tube, the voltage divider chain and a 1 mm thick  $\mu$ -metal shield, extending 30 mm beyond the photocathode surface. To increase the count rate stability active dividers were used, instead of conventional resistive ones. Illustration of TOF1 station is shown in Fig. 2 together with an exploded view of a slab.

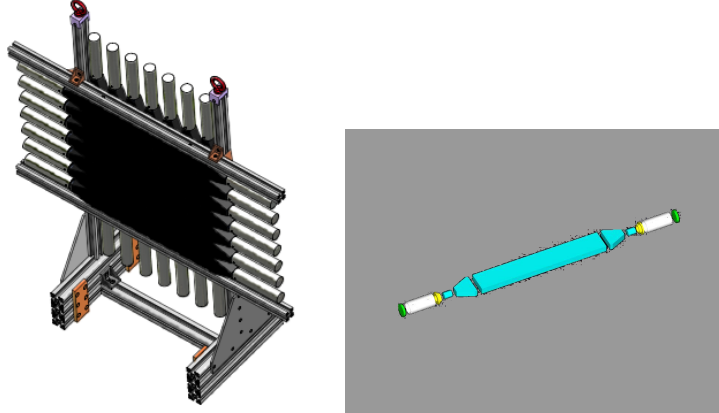


Figure 2: TOF design [9] and slab components [2].

The stations TOF0, TOF1, and TOF2 had active areas of  $40 \times 40 \text{ cm}^2$ ,  $42 \times 42 \text{ cm}^2$ , and  $60 \times 60 \text{ cm}^2$  respectively. Each of the planes in TOF0 station had 10 4-cm wide scintillator slabs. Stations TOF1 and TOF2 used 65 7 and 10 in each plane, respectively. The PMTs are connected to a 50% – 50% passive splitter using  $\sim 34 \text{ m}$  long RG213 signal cable. One half of the signal is fed to the leading-edge CAMAC Lecroy 4115 discriminator followed by CAEN V1290 TDC for time measurements. Second half of the signal goes to CAEN V1724 FADC for pulse-height measurements. Pulse height measurement is instrumental for time-walk corrections. Each station issued a local readout trigger if signals in both PMTs attached to a slab crossed a specific threshold. All 70 three stations were read out when TOF1 station issued a local trigger. This readout trigger was also used for the rest of the MICE detector systems.

All stations were exposed to residual magnetic fields: TOF0 station was placed in a relatively low residual field produced by the last quadrupole magnet of the beam line, while the other two TOF stations were exposed to the stray fields of the cooling channel solenoids. A shielding structure was adopted covering all PMTs at 75 each side of the stations.

The purpose of the TOF system is to effectively discriminate particle species based on time-of-flight measurement. The main components in the MICE beam are muons, pions, and electrons. The time resolution needs to be sufficiently good to effectively discriminate between these types. At 240 MeV/c, the time-of-flight difference between muon and pion is about 1.3 ns between TOF0 and TOF1 stations. With 200 ps resolution, 80 one reaches near 100% discrimination efficiency.

### 2.1.1 Calibration Method

Measurement of time traversal of a particle through a TOF station is influenced by several factors at the hardware level. When a particle crosses the plastic scintillator, there is a short delay in light production, with a characteristic decay time of 1.8 ns.

---

<sup>2</sup>one-inch linear focused PMTs with 10 stages, typical gain  $G \sim 5.7 \times 10^6$  at -2250 V and  $B=0$  T, rise time 0.7 ns, transit time spread (TTS)  $\sim 160$  ps

85 After generation, scintillation light propagates to the ends of each scintillator slab where it is detected by photomultiplier tubes. The light-travel time depends on the distance of the particle crossing from the PMT. The lengths of slabs in TOF0, TOF1, and TOF2 were 40 cm, 42 cm, and 60 cm, respectively. This translates to about 3 ns, 3.1 ns, and 4.4 ns, respectively, as the effective light propagation speed in the scintillator was found to be approximately 13.5 cm/ns.

90 More delay was introduced by the transit time of each PMT and of the cable that led the signal to the readout electronics. These times were unique for each individual PMT channel and needed to be determined in dedicated measurements.

95 The times of each signal of a PMT were measured as times of signal threshold crossings in a simple linear discriminator. This introduced bias in the measured time dependent on the total charge of the signal, effect referred to as time-walk.

100 Signal times of each channel were recorded in TDC boards. Readout of the whole system was triggered by having a signal in TOF1 station. The readout trigger signal is distributed to all TDC boards and is used as a reference time. Which PMT channel's threshold crossing caused the readout was depending on where the particle crossed through the TOF1 station. As a consequence, the reference time had a bias dependent on the position of TOF1 crossing, an effect referred to here as trigger delay.

The final time measurement in each station was determined as an average of the times of individual channels. This way, different distance from the point of crossing to each side of the scintillator slabs does not matter anymore, because the average of the times of the 2 PMTs does not depend on it.

105 Corrections which need to be made to the measured times are then the time-walk correction, the PMT channel specific delay time  $T_0$ , and a correction for the reference trigger time delay.

Details of the calibration method are described in [10].

### 2.1.2 Reconstruction

110 Particle crossing a TOF station must have crossed 2 orthogonal slabs in the stations 2 planes. The time and approximate position of particle crossing a TOF station was reconstructed from the PMT signals in the two slabs. Each slab with at least one recorded signal in each of the 2 attached PMTs was considered as being crossed by a particle. Times of these recorded signals were corrected for time-walk, readout trigger signal delay, and the channel specific delay. Time of crossing of the slab was then taken as the average of the 2 corrected PMT times.

115 The 2 slabs hit by a particle defined a pixel of area given by the width of the slabs. Sometimes, there were more slabs in each plane with signals. Matching of 2 slabs being crossed by a particle was done based on their measured signal time. They were matched if the times were within a 4-ns window. The time of the particle crossing was determined as the average of times of the 2 matched slabs.

120 In order to be able to correct for the trigger signal delay, the pixel through which the particle crossed TOF1 needed to be determined. All possible combinations of 2 slabs from 2 different planes were tested. The times of the recorded PMT signals were corrected under the hypothesis that correct slabs were matched. The pixel of the crossing particle was identified if the time difference of the 2 slabs was shorter than 4 ns.

## 2.2 Performance

125 Resolution of time-of-flight measurement is given by time resolution of each station. The time of a station particle crossing is determined from the average of times of the two slabs. The resolution of the average is a half of the spread of their difference. Therefore, looking at slab  $\Delta T$  allows determination of the time-of-flight resolution.

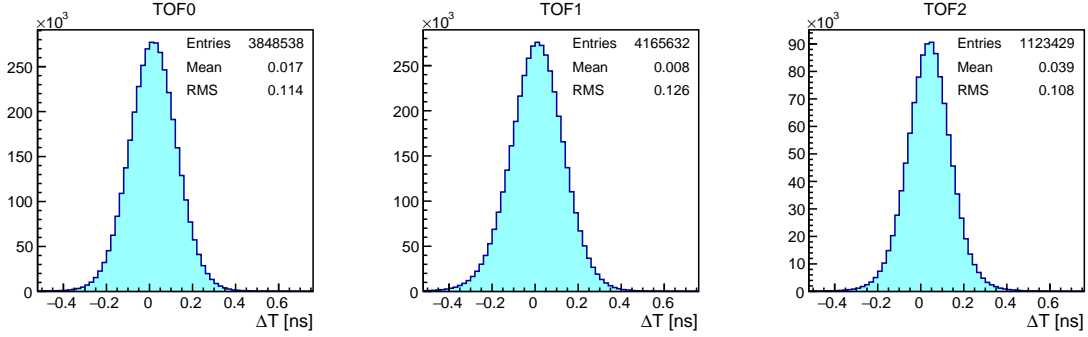


Figure 3: Overall slab  $\Delta T$  distributions. Total width of the distribution is due to the resolution of individual pixels and due to the offsets in their  $\Delta T$  distributions.

Overall performance can be inferred from the combined slab  $\Delta T$  distributions. The plots in Fig. 3 show that they all centre approximately at 0 ns and they exhibit very similar resolutions, with TOF1 having the largest spread.

130 The reconstruction of a pixel by matching of 2 slabs from different planes of each station is dependent on the slab  $\Delta T$ . The 4 ns time window for the matching was chosen to cover the errors of the calibrations. Yet, there were times when there were signals in slabs in each plane of a station, but they were never matched. These events were mostly results of multiple particles passing through the station and causing signal in one plane only. They would never be matched in time as they arrived within the beam bunch time stretch of about 1  $\mu$ s.

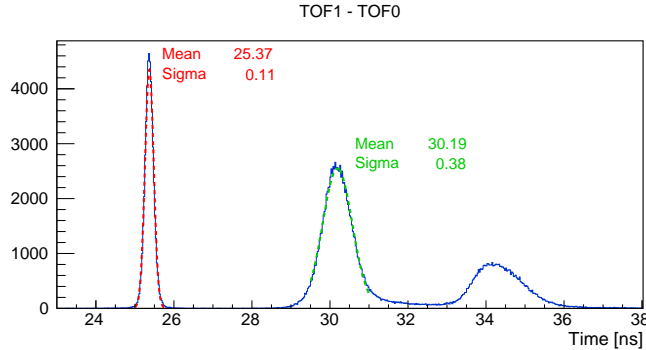


Figure 4: Time of flight between TOF0 and TOF1 for a “pion” beam after all corrections have been applied. From the left: the well separated electron, muon and pion peaks.

### 135 3 Cherenkov Detectors

#### 3.1 Introduction

The MICE Cherenkov threshold detectors, measuring velocity, are primarily designed to provide  $\pi$ - $\mu$  separation in the higher momentum ranges, where TOF peaks separation is not sufficient for conclusive particle identification.

140 In order to provide separation over a large range of momenta, two high density silica aerogel Cherenkov detectors (CkovA and CkovB) with refractive indices  $n=1.07$  and  $n=1.12$  are used. Light is collected in

each counter by four 9354KB eight-inch UV-enhanced phototubes and recorded by CAEN V1731 FADCs (500 MS/s). The two detectors are placed directly one after another in the beamline, located just after the first TOF counter. In Fig. 5 an exploded view of one detector is shown.

Their respective thresholds provide different responses in four distinct momentum ranges, i.e. in the 200 MeV/c beams, pions are below the threshold which would fire the detector for both CkovA and CkovB whereas muons are above only for CkovB, while for the 240 MeV/c beams, pions are above the threshold for CkovB while muons are above for both CkovA and CkovB. Using this information algorithms can be written that produce likelihood distributions of particle type. Below the CkovB muon threshold of about 217.9 MeV/c, where there is no separation, the TOFs provide good separation, whereas the momentum range above the CkovA pion threshold 367.9 MeV/c is outside of the MICE running parameters [11]. For unambiguous identification of particle species the Cherenkov detectors would need a momentum measurement from the MICE Tracker.

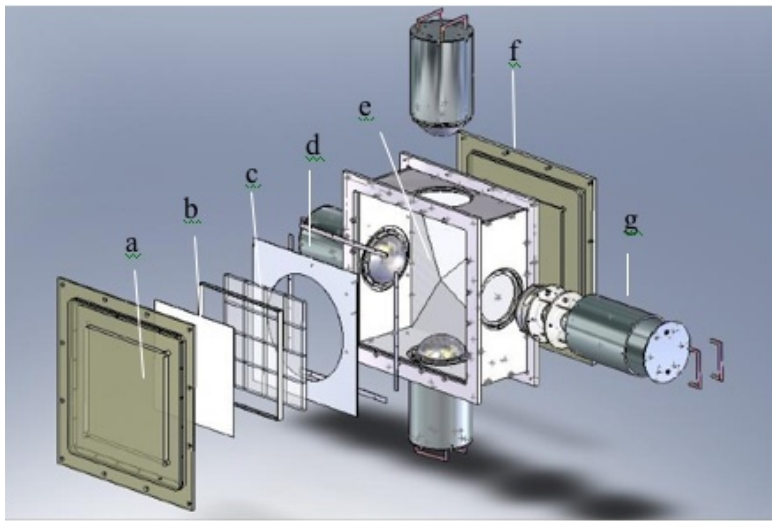


Figure 5: MICE aerogel Cherenkov counter blowup: a) entrance window, b) mirror, c) aerogel mosaic, d) acetate window, e) GORE reflector panel, f) exit window and g) eight-inch PMT in iron shield.

### 3.2 Performance

The data sets used to evaluate the Cherenkov detectors are summarized in Table 1. A wide range of settings (including alignment runs) has been used in order to cover the full spectra of particles that could have been measured by the detectors.

The asymptotic light yield (for  $\beta=v/c=1$ ) in each counter has been measured using the electron peaks, giving  $16 \pm 1$  photoelectrons (NPE) in CkovA and  $19 \pm 1$  in CkovB.

The photoelectrons yields versus momentum for muons and pions in CkovA and CkovB are displayed in Fig. 6, using the time of flight between TOF0 and TOF1 to select the species and estimate the momenta. The distributions of NPEs as a function of the momentum P have been fitted with the function

$$NPE(P) = NPE_0 + NPE_{\beta=1} \left( 1 - \left( \frac{P_0}{P} \right)^2 \right) \quad (1)$$

where  $NPE_0$  is the number of background photoelectrons,  $NPE_{\beta=1}$  is the asymptotic light yield and  $P_0$  is the momentum threshold.

Run ID	Date	Nominal momentum [MeV/c]	Spills	Triggers
10488	12/12/2017	140	3777	300269
10496	12/12/2017	170	4180	371037
10391	03/12/2017	200	2146	240033
10419	04/12/2017	240	2932	328062
10304	29/11/2017	300	2502	305363
10221	23/11/2016	300	4493	560119
10519	15/12/2017	400	4316	506384

Table 1: Summary of the data sets used to visualize the activation curve of the MICE Cherenkov detectors.

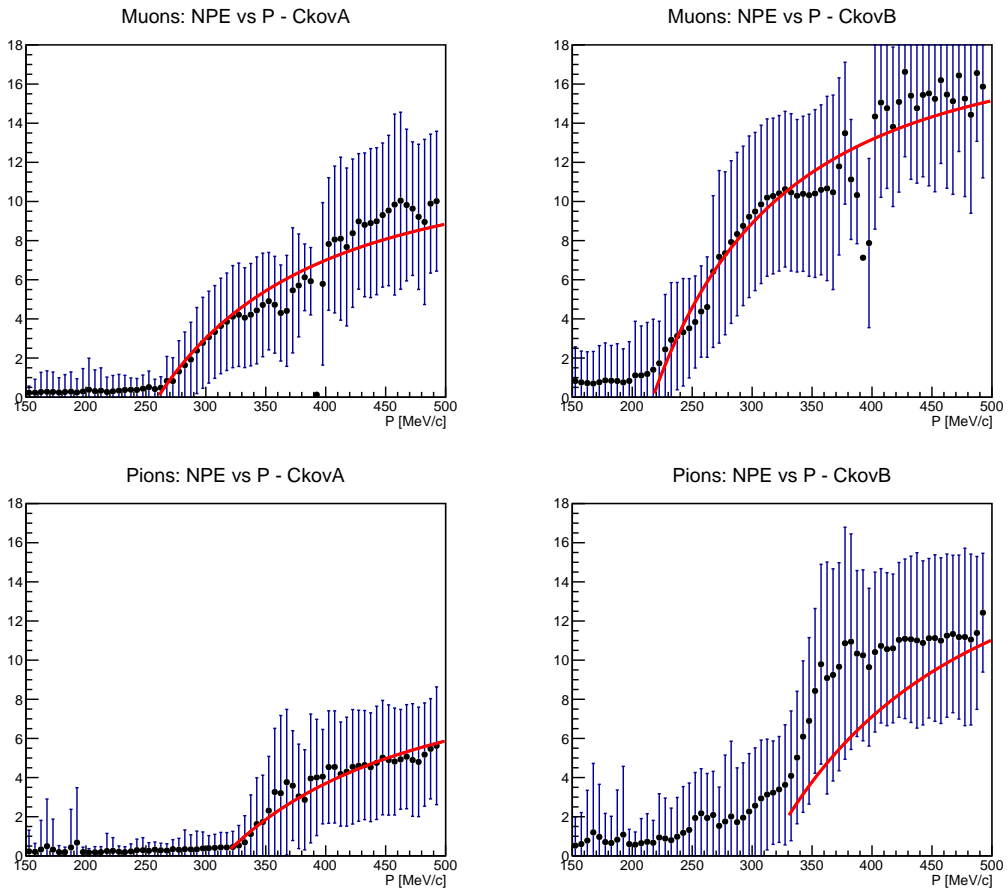


Figure 6: Photoelectron yields versus momentum for muons and pions in CkovA and CkovB with the superimposed fitted activation functions. The error bars correspond to the standard deviation for each momentum bin.

The observed muon thresholds are  $267.3 \pm 18.1$  and  $219.4 \pm 14.5$  MeV/c, while for pions are  $332.2 \pm 38.4$  MeV/c and  $295.9 \pm 95.9$  MeV/c, respectively in CkovA and CkovB. The  $NPE_{\beta=1}$  values are generally lower than the values predicted as in a previous analysis [11] done with Step I data: this is mostly due to TOF0 acting as a pre-shower radiator.

In Fig. 7 is shown the typical photoelectron spectra for muons and pions well above the threshold. The expected Poisson-like distribution receives tails from the electromagnetic showers and from secondary electrons

170 coming from interactions in TOF0 and in the aerogel itself.

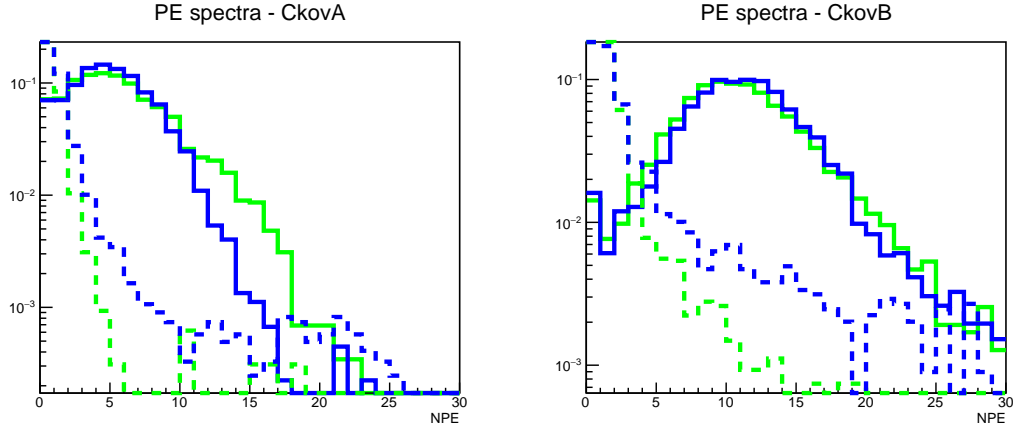


Figure 7: Photoelectron spectra in CkovA (left) and CkovB (right) for muons (green) and pions (blue) above (continuous line) and below (dashed line) the threshold. The distributions are normalised.

## 4 KLOE-Light Calorimeter

### 4.1 Introduction

The KLOE-Light (KL) pre-shower sampling calorimeter is composed of extruded lead foils in which scintillating fibres are placed in volume ratio scintillator:lead  $\sim 2:1$ , “lighter” than the one of the KLOE experiment calorimeter (1:1).

The fibres are 1 mm diameter BICRON BCF-12, scintillating in the blue, 1.35 mm distant from each other within a layer. The distance between two layers is 0.98 mm, one layer being shifted by half the fibre pitch with respect to the next. Scintillation light is guided from each slab into a total of six PMTs (three on each side). Iron shields are fitted to each photomultiplier to mitigate against large stray magnetic fields from the cooling 180 channel. The signal from each PMT is sent to a shaping amplifier (SA) module, which shapes and stretches the signal in time in order to match the sampling rate of the flash ADCs (Fig. 8 shows the design of a single slab). A total of 7 slabs forms the whole detector, which has an active volume of  $93\text{ cm} \times 93\text{ cm} \times 4\text{ cm}$ .

With its 2.5 radiation lengths the KL is used to distinguish muons from decay electrons providing energy deposition and timing information and to act as pre-shower in front of the EMR. The detector has been used to 185 estimate the level of pion contamination within the MICE muon beams to be around 1% [8].

### 4.2 Performance

The study of KL response to different particle types at different momenta is based on particle identification obtained by time-of-flight detector, as shown in the example of Fig. 4, by applying proper cuts on the time-of-flight spectrum. The performance is presented for 140, 170, 200, 240 and 300 MeV/c momenta at the absorber 190 position, and depending of species population for muons, pions and electrons. The results presented below are obtained from the straight tracks data (i.e. without magnetic fields in the trackers or focus coil) taken mainly in 2017. The KL response to muons, pions and electrons for all available momenta is presented in Fig. 9. It is

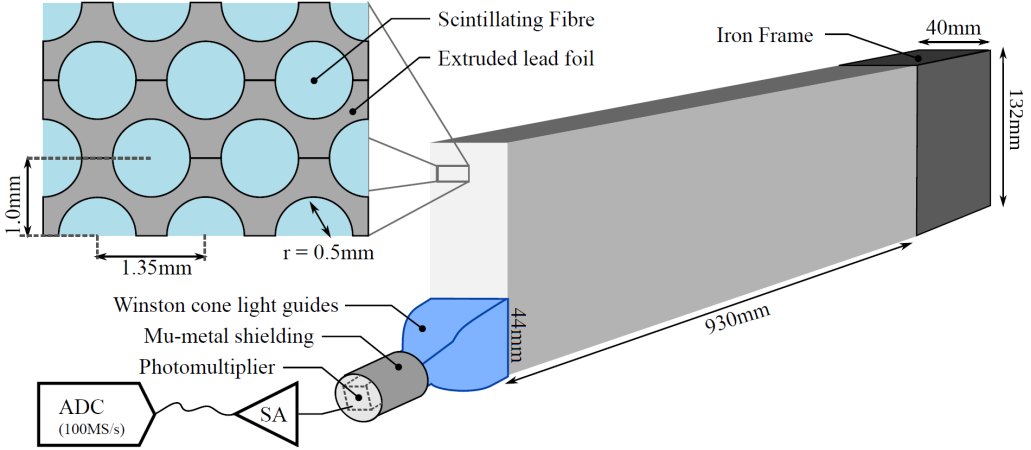


Figure 8: Single slab design of MICE KLOE-Light Calorimeter.

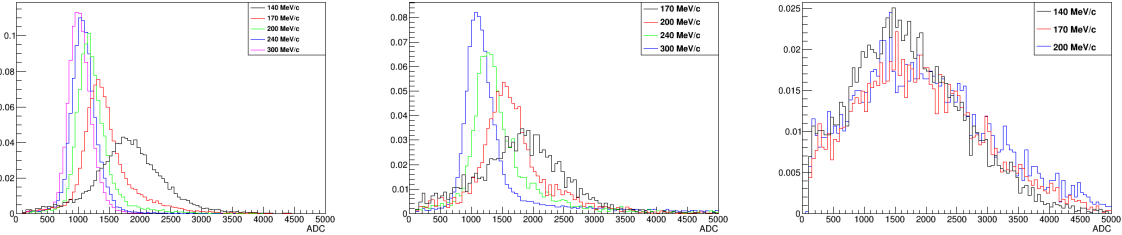


Figure 9: KL response to muons (left), pions (centre) and electrons (right) for several momenta. It is shown charge deposited by particles in KL in arbitrary units. All histograms are normalized to unity.

clear in the cases of muons and pions that they are below mip momenta since energy deposition decreases with momentum increasing<sup>3</sup>.

For comparison of energy deposition of muon, pions and electrons for fixed momentum Fig. 10 is presented. In the case of 300 MeV/c (Fig. 10, right), where muons and pions have almost the same maximum of distribution, the tail of pions is fatter than muon one. This is due to the fact that pions experience strong interaction as well. This pion behaviour has been used to estimate its contamination in muon sample.

The number of fired KL cells by a single muon, electron or pion is given in Fig. 11 for 240 MeV/c beam. For muons we expect one, in some cases two and almost never more fired cells depending on track inclination. Pions and electrons create avalanches in KL and electron ones is much wider than the pion ones as visible of number of KL cell hits. The same figure shows number of events when if there is a reconstructed TOF track, but no signal in KL above the threshold. This can be used to calculate efficiency of KL for the three species as a function of momentum. The results are presented in Table 2 and shows that efficiency for muon registration is close to 99%.

In Fig. 12 is shown simulation of KL response to 300 MeV/c muons and pions and the distributions are compared with data. The agreement between data and simulation is very good. The simulation is done via following steps:

<sup>3</sup>Actually the energy deposition is defined as the sum of ADC products from all cells in KL above a given threshold. The ADC product on the other hand is the product of left and right side of one slab divided by the sum of left and right side:  $ADC_{prod} = 2 \times ADC_{left} \times ADC_{right} / (ADC_{left} + ADC_{right})$ . The factor 2 is present for normalization. The product of two sides compensates the effect of attenuation.

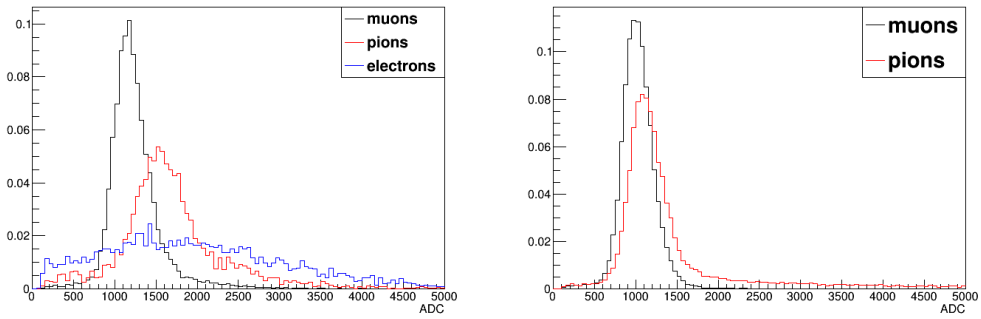


Figure 10: Comparison of energy deposition of muons, pions and electrons at 200 MeV/c (left) and of muons to pions at 300 MeV/c (right).

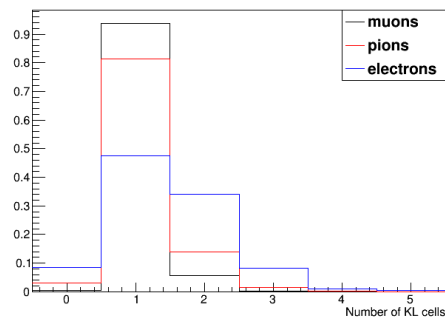


Figure 11: Particle multiplicity for 240 MeV/c, i.e. number of KL cells fired.

<b>species</b>	<b>140 MeV/c</b>	<b>170 MeV/c</b>	<b>200 MeV/c</b>	<b>240 MeV/c</b>	<b>300 MeV/c</b>
<b>electrons</b>	$0.95 \pm 0.02$	$0.95 \pm 0.01$	$0.94 \pm 0.03$	n/a	n/a
<b>muons</b>	$0.97 \pm 0.02$	$0.99 \pm 0.01$	$0.99 \pm 0.01$	$0.99 \pm 0.01$	$0.99 \pm 0.01$
<b>pions</b>	n/a	$0.89 \pm 0.03$	$0.95 \pm 0.03$	$0.97 \pm 0.03$	$0.98 \pm 0.01$

Table 2: Efficiency of KL for electrons, muons and pions as a function of particle momentum. The conditions required are existing of a TOF track and signal in KL above the threshold. The uncertainties are statistical.

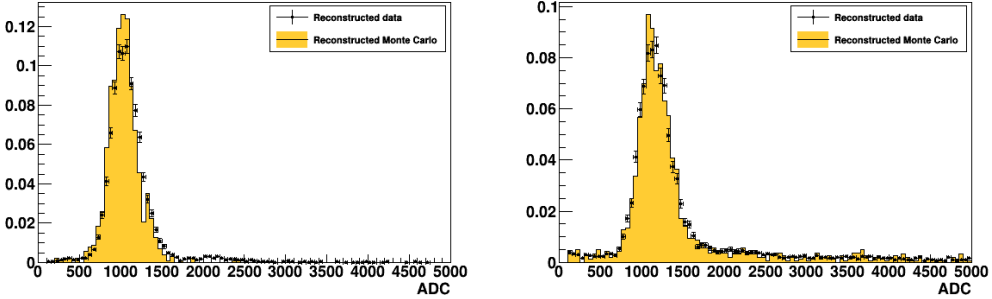


Figure 12: Comparison between data and Monte Carlo simulation of KL response to muons (left) and pions (right) at 300 MeV/c.

- Smearing of produced photons in scintillator fibres. They obtain Poisson statistic so such is applied. In principle one can replace it with Gaussian because the number of photons created is large enough for such an approximation.
- Photoelectrons created on photomultiplier photocathode also have Poisson statistics. It cannot be replaced here with normal distribution because the number of photoelectrons is small enough so such an approximation is illegal.
- Photomultiplier gain obtains also statistical properties but it is neither Poisson nor gauss. Nevertheless it turns out that for simplicity one can use Gaussian distribution with mean value equals to PMT gain and sigma of distribution equals to half of the gain. KL photomultipliers have gain  $\sim 2 \times 10^6$ , so their sigma is simply  $10^6$ .

## 5 Electron Muon Ranger

### 5.1 Introduction

The Electron-Muon Ranger (EMR) is a fully-active scintillator detector [12]. It can be classified as a tracking-calorimeter as its granularity allows for track reconstruction. The EMR consists of extruded triangular scintillator bars arranged in planes. One plane contains 59 bars and covers an area of  $1.27 \text{ m}^2$ . Each even bar is rotated by 180 degrees with respect to the odd one. A cross-section of bars and their arrangement in a plane is shown in Fig. 13. This configuration does not leave dead area in the detector for particles crossing a plane with angles that do not exceed 45 degrees with respect to the beam axis. Each plane is rotated through 90 degrees with respect to the previous one, such that a pair of planes defines a horizontal and vertical ( $x, y$ ) interaction coordinate. The light, produced when a particle crosses a bar, is collected by a wave-length shifting (WLS) fibre glued inside the bar. At both ends, the WLS fibre is coupled to clear fibres that transport the light to a

230 photomultiplier tube (PMT). Signals produced in a plane are read out collectively on one end by a single-anode PMT for an integrated charge measurement and separately on the other by a multi-anode PMTs for individual bar hit reconstruction. The full detector is composed of 24 X-Y modules for a total active volume of  $\sim 1 \text{ m}^3$ .

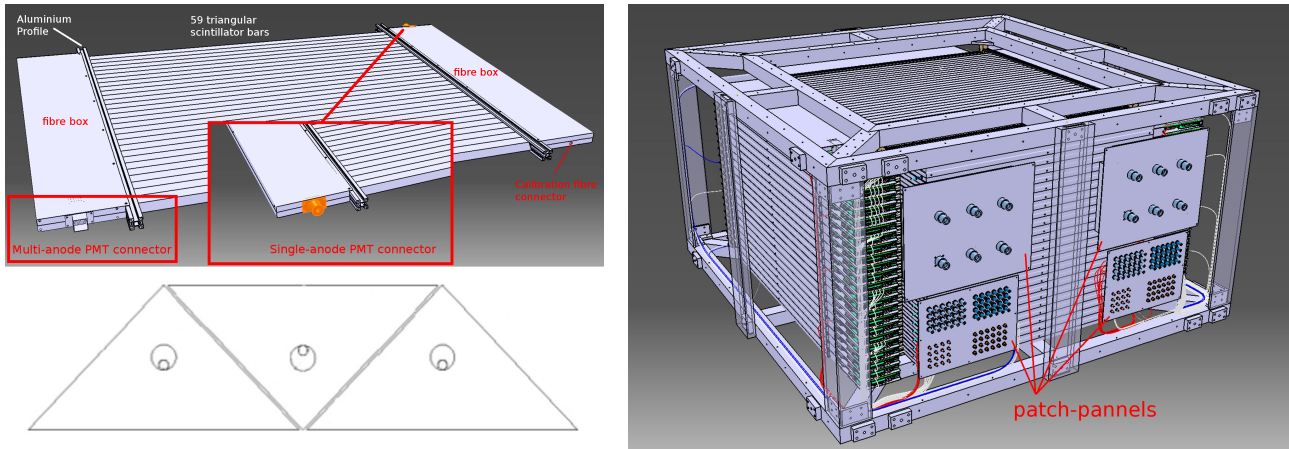


Figure 13: Drawing of one EMR plane (top left), cross section of 3 bars and their wavelength shifting fibres (bottom left) and drawing of the full detector and its supporting structure (right).

An array of analyses were conducted to characterize the hardware of the EMR and determine whether the detector performs to specifications [13]. The clear fibres coming from the bars were shown to transmit the  
235 desired amount of light, and only four dead channels were identified in the electronics. The level of crosstalk is within acceptable values for the type of multi-anode photomultiplier used with an average of  $0.20 \pm 0.03\%$  probability of occurrence in adjacent channels and a mean amplitude equivalent to  $4.5 \pm 0.1\%$  of the primary signal intensity. The efficiency of the signal acquisition, defined as the probability of recording a signal in a plane when a particle goes through it in beam conditions, reached  $99.73 \pm 0.02\%$ .

240 The primary purpose of the EMR is to distinguish between muons and their decay products, identifying muons that have crossed the entire cooling channel. Muons and electrons exhibit distinct behaviours in the detector. A muon follows a single straight track before either stopping or exiting the scintillating volume, while electrons shower in the lead of the KL and create a broad cascade of secondary particles. Two main geometric variables, the plane density and the shower spread, are used to differentiate them. The detector  
245 is capable of identifying electrons with an efficiency of 98.6 %, providing a purity for the MICE beam that exceeds 99.8 %. The EMR also proved to be a powerful tool for the reconstruction of muon momenta in the range 100–280 MeV/c [14].

## 5.2 Performance

The performance of the EMR detector is assessed at three levels of resolution with the data acquired during the  
250 2017/02 and 2017/03 ISIS user cycles. The performance of the hardware itself is evaluated by analysing the characteristics of raw photomultiplier signals. The reconstruction efficiency is assessed by looking at higher level quantities. The performance of the detector as an electron tagging device is measured.

### 5.2.1 Hardware efficiencies

The data sets used to evaluate the detector hardware efficiencies are summarized in table 3. The MICE beam line is tuned to the highest attainable momentum to maximize the transmission to the EMR detector and increase the range of particles in the detector. In this configuration, the beam line produces pions and muons in comparable quantities, along with positrons. The particle species are identified by evaluating their time-of-flight between TOF1 and TOF2. Only the particles with a time-of-flight between 28 and 28.75 ns, i.e. compatible with the muon hypothesis, are included in the analysis sample.

Run ID	Date	Type	Momentum	Spills	Triggers	EMR events
9619	19/09/2017	$\pi^+$	400 MeV/c	2289	265312	36775
9620	19/09/2017	$\pi^+$	400 MeV/c	5388	668026	107578
<b>Total</b>				7677	933338	144353

Table 3: Summary of the data sets used to measure the efficiency of the EMR in the 2017/02 ISIS user cycle.

A muon that makes it into the analysis sample has a momentum larger than  $350 \text{ MeV}/c$  right before TOF2. It is expected to cross both TOF2 and the KL without stopping and penetrate the EMR. In practice, the probability of creating an EMR event, i.e. to produce hits in the detector is  $99.62 \pm 0.03\%$ . The minor inefficiency may be attributed to pions in the muon sample that experience hadronic interactions in the KL. If hits are produced in the detector, space points are reconstructed  $98.56 \pm 0.06\%$ . This inefficiency may be associated with muon that decay between TOF2 and the EMR and produce scarce hits in the detector.

To evaluate the efficiency of the scintillator planes and their readouts, only the muons which penetrate the entire detector are taken into account. If a signal is recorded in the most downstream plane, it is expected that at least a bar will be hit in each plane on its path and that a signal will be recorded in the single anode PMT. In  $3.26 \pm 0.02\%$  of cases, on average, a plane traversed by a muon will be not produce a signal in its MAPMT and that the most probable amount of bars hit is one, while a track is missed by an SAPMT  $1.88 \pm 0.01\%$  of the time. Figure 14 shows the probability of recording a signal in individual MAPMTs and the SAPMTs for each of the 48 planes, given a muon that crosses the whole detector. The most inefficient PMTs miss the track  $\sim 10\%$  of the time.

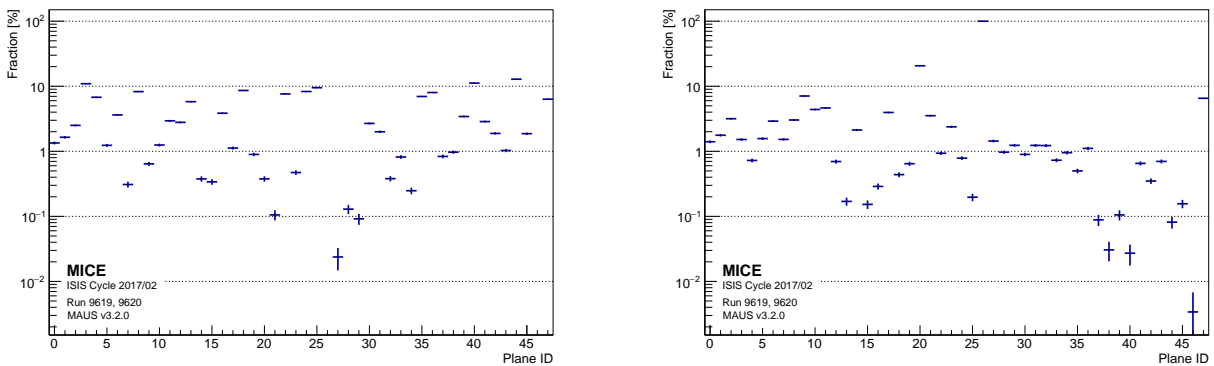


Figure 14: Probability of not producing a single bar hit in the MAPMT (left) and a zero charge in the SAPMT (right) in the 48 individual EMR planes.

### 5.2.2 Electron rejection

- 275 The main purpose of the Electron-Muon Ranger is to tag and reject the muons that have decayed in flight inside  
the experimental apparatus. A broad range of beam line momentum settings, summarized in table 4, is used to  
characterize its muon selection efficiency. The particle species are characterized upstream of the detector by  
using the time-of-flight between TOF1 and TOF2 as shown before. The limits of the peaks are fitted to each  
setting in order to separate the muons and positrons into two templates upstream of the EMR. Particles that fall  
280 above the upper limit of the muon peak are either pions or slow muons and are rejected from this analysis.

Run ID	Date	Type	Momentum	Spills	Triggers	EMR events
10268	26/11/2017	$\pi^+$	170 MeV/c	4418	328948	97452
10269	26/11/2017	$\pi^+$	170 MeV/c	3695	278330	82098
10262	25/11/2017	$\pi^+$	200 MeV/c	846	28103	8769
10266	25/11/2017	$\pi^+$	200 MeV/c	4365	148990	45448
10267	26/11/2017	$\pi^+$	200 MeV/c	4296	194207	53469
10275	26/11/2017	$\pi^+$	200 MeV/c	3547	126597	39114
10261	25/11/2017	$\pi^+$	240 MeV/c	4388	228337	66335
10264	25/11/2017	$\pi^+$	240 MeV/c	755	32322	10041
10265	25/11/2017	$\pi^+$	240 MeV/c	3336	134953	43129
10270	26/11/2017	$\pi^+$	240 MeV/c	222	17584	4030
10271	26/11/2017	$\pi^+$	240 MeV/c	66	5063	287
10272	26/11/2017	$\pi^+$	240 MeV/c	177	13538	1967
10273	26/11/2017	$\pi^+$	240 MeV/c	4339	232488	67350
10274	26/11/2017	$\pi^+$	240 MeV/c	738	38734	11123
<b>Total</b>			35188	1808194	530612	

Table 4: Summary of the data sets used to measure the efficiency of the EMR in the 2017/02 ISIS user cycle.

MICE is a single-particle experiment, i.e. the signals associated with a trigger originate from a single particle traversing the detector. The multi-anode readout of each detector plane provides an estimate of the position of the particle track in the  $xz$  or the  $yz$  projection, depending on the orientation of the scintillator bars. Inside the detector the muon exhibits a clean straight track while the positron showers inside the lead of the KL and produces a disjointed and widespread signature. Two particle identification variables based on these distinct characteristics can be defined. One is the plane density,  $\rho_p$ , defined as

$$\rho_p = \frac{N_p}{Z_p + 1}, \quad (2)$$

with  $N_p$  the number of planes hit and  $Z_p$  the number of the most downstream plane. A muon deposits energy in every plane it crosses until it stops, producing a plane density close or equal to one. A positron shower contains photons that may produce hits deep inside the fiducial volume without leaving a trace on their path, reducing the plane density. The second variable is the normalised chi squared,  $\hat{\chi}^2$ , of the fitted straight track, i.e.

$$\hat{\chi}^2 = \frac{1}{N - 4} \sum_{i=1}^N \frac{\text{res}_{x,i}^2 + \text{res}_{y,i}^2}{\sigma_x^2 + \sigma_y^2}, \quad (3)$$

with  $N$  the number of space points (one per bar hit),  $\text{res}_{q,i}$  the residual of the space point with respect to the track in the  $qz$  projection and  $\sigma_q$  the uncertainty on the space point in the  $qz$  projection,  $q = x, y$  [15]. The number of degrees of freedom is  $N - 4$ , as a three-dimensional straight track admits four parameters. This

quantity represents the transversal spread of the particle's signature. A muon follows a single track and is expected to have a  $\hat{\chi}^2$  close to one, while an electron shower is expected to produce a larger value. The two discriminating variables can be combined to form a statistical test on the particle hypothesis. Given an unknown particle species, consider a set of cuts,  $(\rho_c, \hat{\chi}_c^2)$ , such that

$$\begin{aligned}\rho_p > \rho_c \cap \hat{\chi}^2 < \hat{\chi}_c^2 \rightarrow \mu^+; \\ \rho_p < \rho_c \cup \hat{\chi}^2 > \hat{\chi}_c^2 \rightarrow e^+.\end{aligned}\quad (4)$$

Dense and narrow events will be tagged as muons while non-continuous and wide electron showers will not.

The quality of a test statistic may be characterized in terms of the loss,  $\alpha$ , the fraction the muon sample that is rejected, and the contamination,  $\beta$ , the fraction of the electron sample that is selected.

The downstream tracker (TKD) allows for the reconstruction of each particle momentum before entering the EMR. To assess the influence of momentum on contamination and loss, their values are calculated for 10 MeV/c bins in the range 100–300 MeV/c. The test statistic performed in each bin is based on the optimal set of cuts optimized for the whole sample, i.e.  $\rho^* = 86.131\%$  and  $\hat{\chi}^{2*} = 14.229$ . Figure 15 shows the loss,  $\alpha$ , and the contamination,  $\beta$ , as a function the TKD momentum. It shows that, at low momentum, the apparent muon loss increases. This is due to an increase in decay probability between TOF2 and the EMR and an decrease in the amount of muons that cross the KL to reach the EMR.

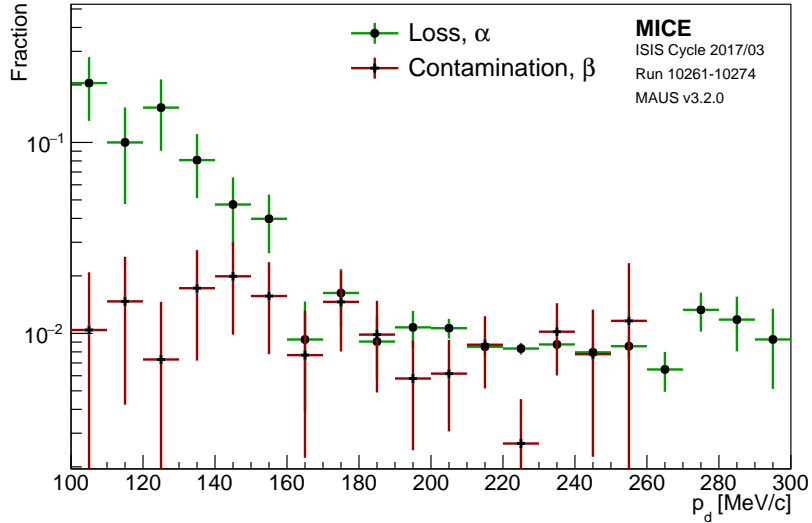


Figure 15: Percentage of electron contamination,  $\beta$ , and muon loss,  $\alpha$ , for different ranges of momentum measured in the downstream tracker,  $p_d$ . The error bars are based on the statistical uncertainty in a bin.

## 6 Trackers

### 6.1 Introduction

MICE is equipped with two identical, high precision scintillating-fibre trackers, described in [16]. Each tracker is placed in a superconducting solenoid designed to provide a uniform magnetic field over the tracking volume. One tracker, TKU, is upstream of the cooling cell, the other, TKD, is downstream, the mirror image of TKU as in Fig. 1.

The trackers are 110 cm in length and 30 cm in diameter (see Fig. 16). There are five stations per tracker (labelled 1 to 5, with station 1 being closest to the cooling cell) held in position using a carbon-fibre space-frame. The stations sit at varying separations in  $z$  (beam axis) of 20–35 cm: this ensures that the azimuthal rotation of track position from one station to the next differs, difference being important in resolving ambiguities at the pattern-recognition stage. Each tracker is instrumented with an internal LED calibration system for calibration and four 3-axis Hall probes to monitor the field.

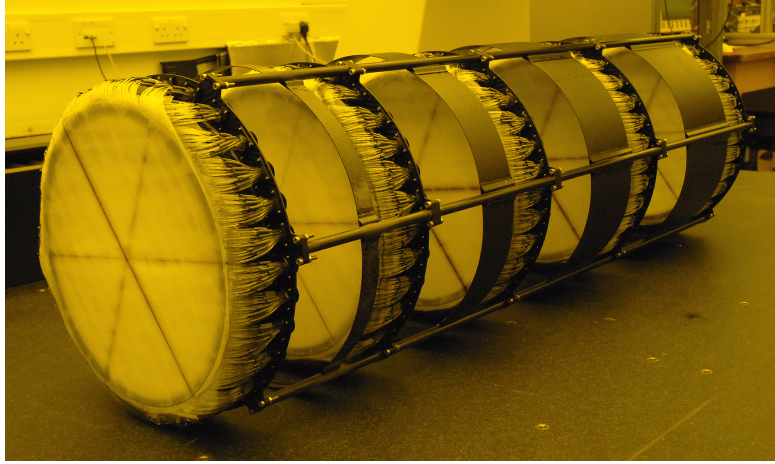


Figure 16: Photograph of one of the MICE Trackers, showing the five stations and the three doublet planes of scintillating fibres, each plane at  $120^\circ$  angles to the next (the central fibres of plane can be seen as darker lines traversing the station). Bundles of seven  $350\mu m$  fibres are grouped together, to be read out by 1 mm scintillating fibre light guides.

The tracker stations consists of three doublet layers of  $350\mu m$  scintillating fibres, these layers are arranged such that each is at an angle of  $120^\circ$  to the next. This arrangement ensures that there are no inactive regions between adjacent fibres. Bundles of seven fibres are grouped into a single readout channel (this reduces the number of readout channels, while maintaining position resolution). The trackers have a spatial resolution per doublet layer of  $470\mu m$  and an expected light yield of  $\sim 10$  photo-electrons.

The light from the seven scintillating fibres passes into a single clear fibre, which takes it to a visible light photon counter (VLPC) which operate at 9 k. The signals from the VLPCs are digitised using electronics developed by the D0 collaboration [17].

## 6.2 Performance and Reconstruction

Each of the 15 tracker planes (three per station and five stations) consist of 214 channels, labelled 0–213, likewise each plane is assigned an integer plane number 0–2. Particle signals are recorded by the tracker electronics and calibrated channel by channel then converted into signal NPE. This information is then used to form a digit and is the first step in tracker reconstruction. Digit profiles are useful in identifying and rectifying or removing hot or dead channels in the planes and ensuring the accuracy of calibration. Smooth centrally peaked spectra are expected in a plane with no dead channels and minimal electronics noise, but this is not an essential requirement since it is the combination of two or three planes which go to make a point in the track and so there is redundancy built in. Hence a significant proportion of individual channels can be lost without a knock on drop in efficiency. The clustering algorithm loops over every combination of pairs of digits in a single event and combines any that occur in neighbouring channels. In the case of a multi-digit cluster, the

unweighted average channel value is used to define the plane coordinate and the NPE is summed.

%endfigure

For each station the constituent planes are searched for clusters that can be used to form a spacepoint. Spacepoints are constructed from clusters from all three planes (a triplet spacepoint) or from any two out of the three planes (a doublet spacepoint).

### 6.2.1 Noise

The scintillating fibre trackers operate by registering digits above a given NPE threshold within each fibre plane. Fibres are collected into channels as ganged bundles of 7 for each channel, with digits registered per channel instead of per fibre. From a coincidence of digit events in 2 or 3 oblique fibres (fibres in differing planes), a spacepoint is reconstructed, from which track reconstruction can occur. We consider noise in the tracker to be those digits registered not from the passage of a beam particle, but instead from other sources, for instance, dark current from thermal electron emission in the PMTs. To isolate noise from signal during beam-on data collection, a strict cut can be made requiring that only events with one fitted track and 5 spacepoints per tracker are selected, with all 5 spacepoints included in the fitted track. All digits corresponding to the track are then removed from the total set of digits for that event, and the remainder are considered noise digits. An in-situ approximation of active channels for the current data-taking period is made, assuming all channels without at least one registered digit in the selected data-taking run are inactive. The average noise rate per channel per event is then calculated as the total number of event digits above the considered NPE threshold in each tracker, divided by both the active channel number and the number of events satisfying the above selection criteria. This gives a value of 0.18% upstream and 0.06% downstream for events above 2 NPE.

### 6.2.2 Track Finding Efficiency

Data were analysed in order to determine the track and spacepoint finding efficiency of the detectors during running conditions. A time-of-flight cut was used to ensure that each measured track had a time-of-flight consistent with a muon throughout the entire experimental apparatus. A hit was therefore required in each of the TOF1 and TOF2 detectors, which ensured that the particle must have been successfully transmitted through the cooling channel, crossing both tracking detectors. These requirements ensure that there is a better than 99.9% probability that a particle will have traversed a tracking detector. The number of events missing a track is therefore measured and used to estimate the efficiency of the detector.

The results of the efficiency analysis are tabulated in table 5 for a range of momentum and nominal emittances. A track-finding efficiency of 98.70% is reported for the upstream tracker and 98.93% for the downstream tracker, averaged over field and beam conditions. Additionally, assuming a track is found, the probability of successfully finding each spacepoint is summarized in table 6. The overall efficiency of both trackers is sufficient to not present any significant systematic uncertainties in the analysis, however it is lower than the ideal expectation, 99.9% efficiency, due to the presence of dead channels, an unavoidable feature of the construction process.

### 6.2.3 Track Fit Predicted Performance

Monte Carlo simulation used with realistic field and beam conditions in order to estimate the reconstruction performance. Run number 09964 was used (140 MeV/c, 10 mm nominal emittance), representing a typical

Momentum	Nominal Emittance	No. Events	Upstream Tracks Found	Downstream Tracks Found
200 MeV/c	6mm	221879	99.42%	96.07%
200 MeV/c	3mm	215229	98.38%	99.19%
140 MeV/c	6mm	180283	98.37%	99.16%
140 MeV/c	10mm	130859	98.47%	98.93%
Averaged		748250	98.70%	98.21%

Table 5: The track finding efficiency for the upstream and downstream trackers for 140 MeV/c and 200 MeV/c beams, and for 3, 6 and 10 mm nominal emittances.

Momentum	Nominal Emittance	No. Events	Upstream Spacepoints Found	Downstream Spacepoints Found
200 MeV/c	6mm	221879	99.41%	94.63%
200 MeV/c	3mm	215229	98.04%	97.41%
140 MeV/c	6mm	180283	97.99%	99.16%
140 MeV/c	10mm	130859	98.07%	97.44%
Averaged		748250	98.44%	97.01%

Table 6: The spacepoint finding efficiency, assuming the presence of a track, for the upstream and downstream trackers for 140 MeV/c and 200 MeV/c beams, and for 3, 6 and 10 mm nominal emittances.

360 data set used for the study of emittance evolution. Results are presented in Fig. 17 for the upstream tracker and Fig. 18 for the downstream tracker.

### 6.3 Efficiency evolution

365 The efficiency of the tracker was processed over the lifetime of its use during the data taking. The analysis used in section 6.2.2 was repeated and automated for runs starting in 2015. The evolution of the helical track finding efficiency in the upstream and downstream trackers is shown in Fig. 19.

## 7 Global Track Matching reconstruction

The overall detector performance can be validated by extrapolating tracks from one detector to another and comparing the reconstructed coordinates with the extrapolated values. Tracks measured in the upstream tracker are extrapolated upstream to TOF1 and TOFO, and downstream to TKD and TOF2. Where there are materials 370 in the beamline, the energy change on passing through the material is estimated using the most probable energy loss. Material thicknesses are approximated by the on-axis thickness.

Asymmetric effects can be introduced due to scattering from the walls of the cooling channel as the beam is not symmetric in the channel. In order to minimise the effects of such scattering, only events whose projected trajectory is significantly distant from the apertures are considered in this analysis. The following sample 375 selection is considered:

- Downstream sample: events must be included in the downstream sample to be considered in this analysis
- Aperture cut: the projected upstream track must be within 100 mm radius from the beam axis at the following apertures: the upstream absorber safety window; the upstream absorber window; the absorber centre; the downstream absorber window; the downstream absorber safety window; the upstream edge of SSD; the Helium window in SSD; the downstream edge of the downstream PRY aperture. This is

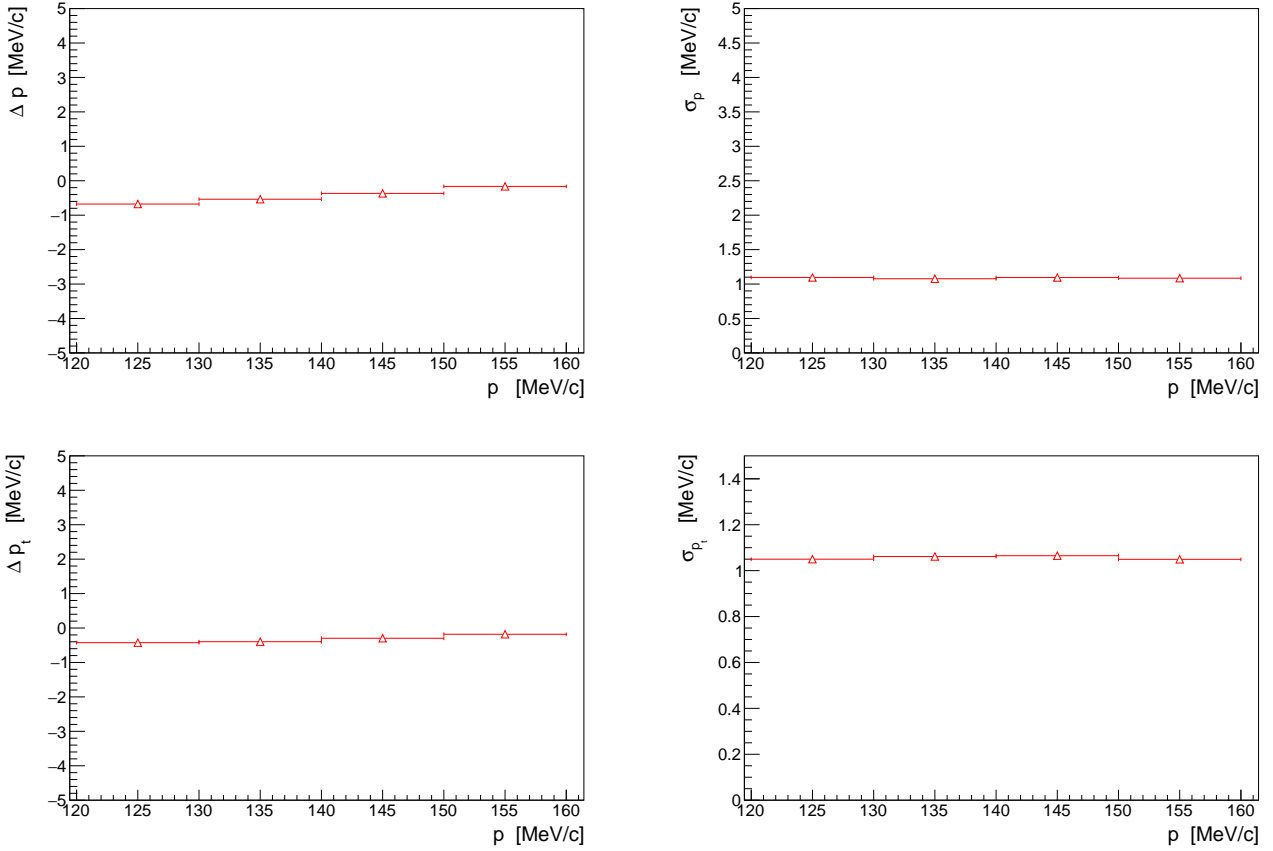


Figure 17: Predicted momentum reconstruction bias (left) and resolution (right) for the longitudinal (top) and transverse (bottom) momentum components in the upstream tracker.

performed even when the IH2 absorber was not installed, for the sake of consistency and because in some instances mounting flanges can limit the aperture and consistency.

- 1 space point in TOF2: the event must have exactly one space point in TOF2.
- Successful track extrapolation to TOF2: the projected upstream track must have been successfully extrapolated to TOF2

385

A typical residual plot is shown in Fig. 20 for the extrapolated position following extrapolation to TOF1. In general the width of the distributions are comparable between MC and data. Where the diffuser is in place for higher emittance beams, the extrapolation goes through the diffuser material so the residuals are wider, owing to the increased scattering from the diffuser.

390 **8 Beam-based detector alignment**

## 8.1 Introduction

To carry out its program, MICE requires all of its detectors to reconstruct space points in a globally consistent fashion. A beam-based alignment algorithm was developed to improve the resolution on the position of the scintillating-fibre trackers lodged inside the bores of superconducting magnets. This method can achieve unbiased measurements of the trackers rotation angles with a resolution of  $6 \text{ mrad}/\sqrt{N}$  and of their position with a resolution of  $20 \text{ mm}/\sqrt{N}$ , with  $N$  the number of selected tracks [18].

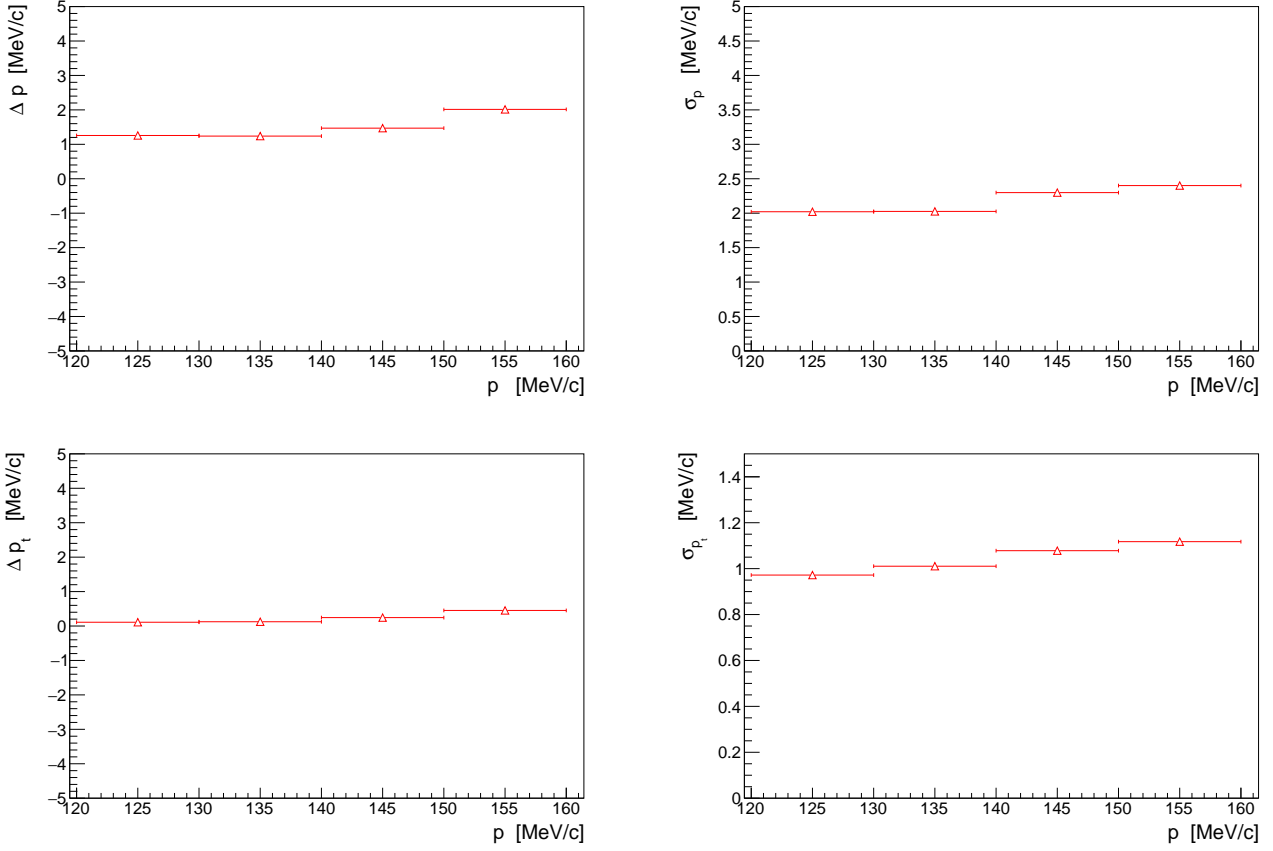


Figure 18: Predicted momentum reconstruction bias (left) and resolution (right) for the longitudinal (top) and transverse (bottom) momentum components in the downstream tracker.

The single-particle nature of the MICE experiment requires reliable global track matching throughout, i.e. the ability to associate a trace measured in the upstream tracker with one in the downstream tracker but also with the particle identification detectors. The many detectors must reconstruct space points in a globally consistent fashion to guarantee reliable and efficient track matching, as well as unbiased muon scattering measurements.

The baseline for the beam-based alignment is the surveys of the detectors in the hall using laser telemetry, performed regularly throughout the commissioning and data taking, following any mechanical activity performed on the beam line and cooling channel. Only the trackers, nested in the superconducting solenoids, could not be accessed, so their position is inferred with respect to the flanges and the beam can be used to check the tracker stations alignment.

## 8.2 Analysis method

The position of each tracker in global coordinates is entirely defined by the location of its centre and a set of three angles. Since the coordinate of each tracker along the beamline is known to great accuracy from the survey and the rotation about  $z$  has negligible influence on the alignment only 4 constants have to be find for each tracker.

The location of the TOFs is used as the reference for the tracker alignment. The line that joins the centre of TOF1 with the centre of TOF2 is chosen to be the reference axis. A deviation from this axis is considered as a misalignment of the trackers. Multiple scattering in the beam line does not allow to do the alignment on single particle basis but works for a larger sample of particles. The mean residual angles and positions of the trackers

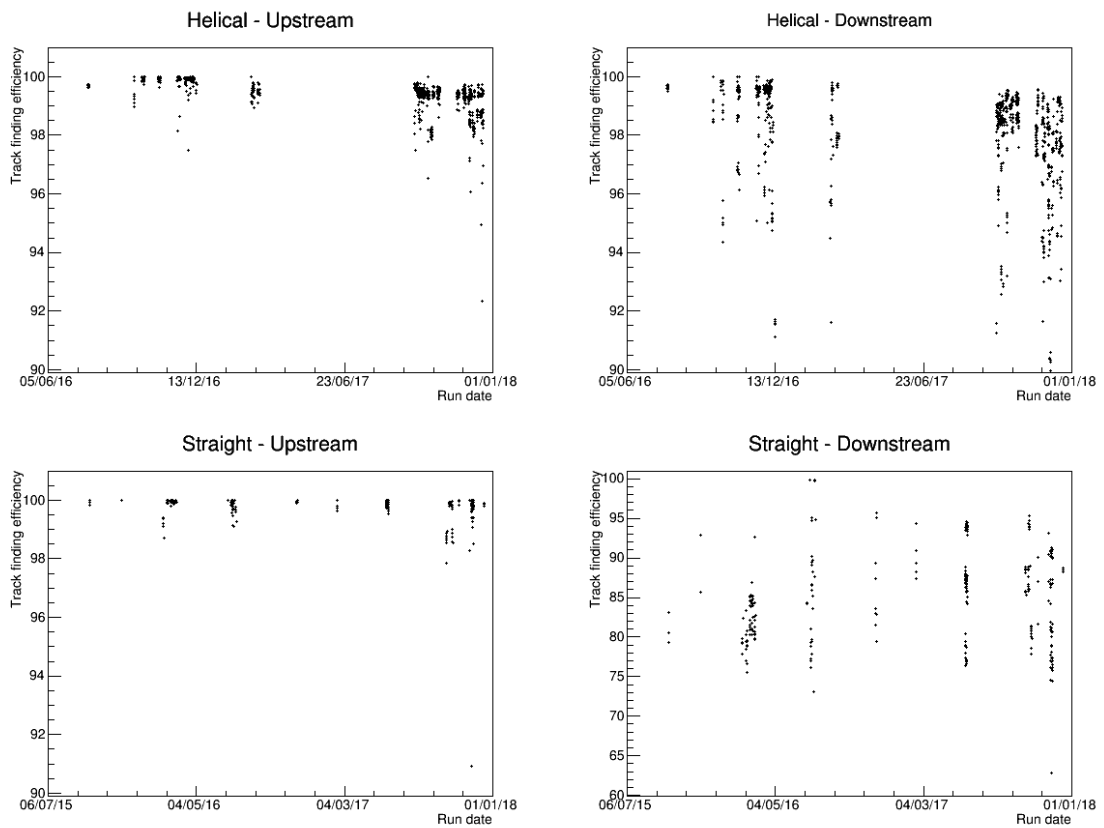


Figure 19: Evolution of the straight and helical track finding efficiency over time for the upstream (left) and downstream (right) trackers during the key periods of data taking since 2016.

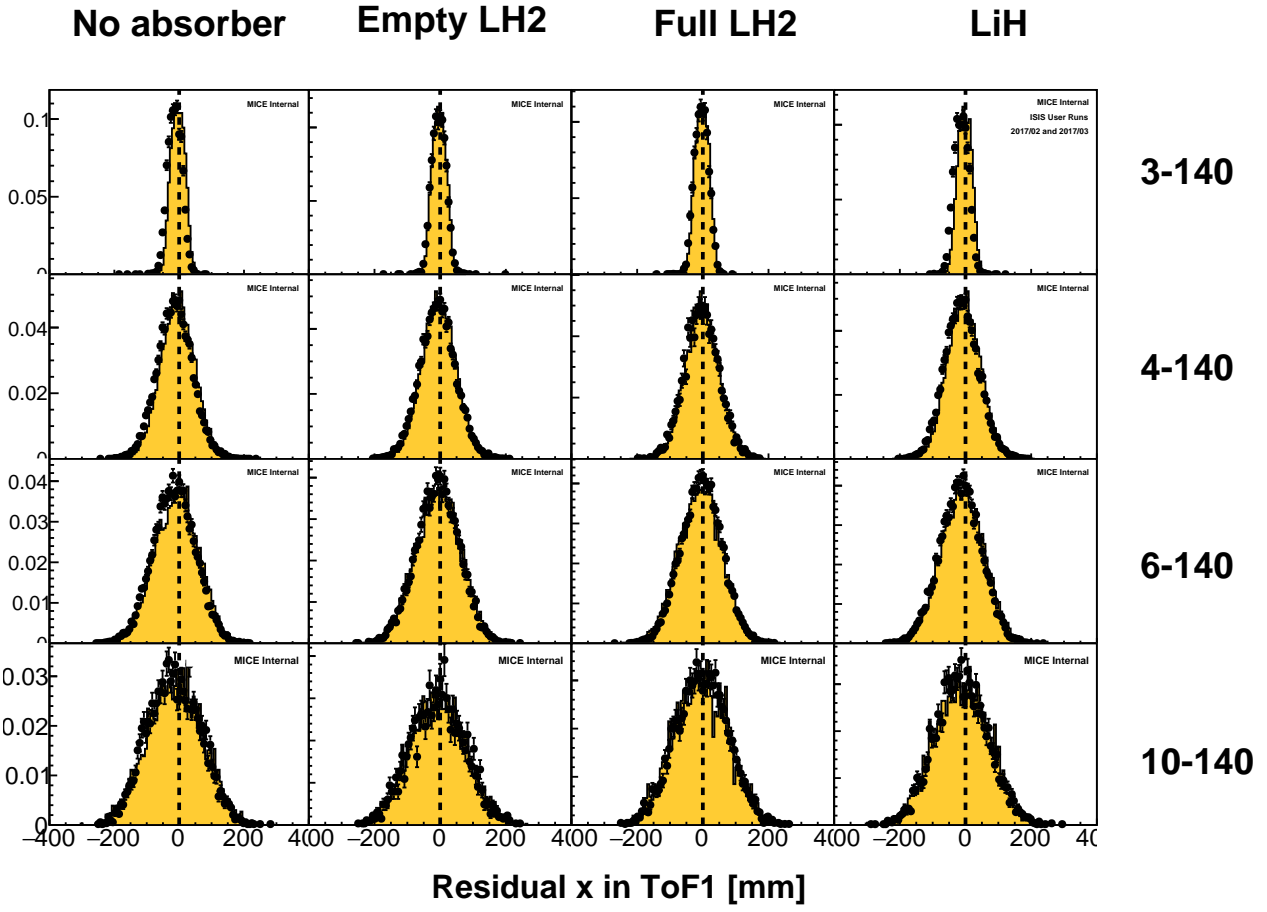


Figure 20: Residual horizontal (x) position in TOF1 of tracker tracks following extrapolation from TKU.

415 with respect to the TOF12 axis are an essential and powerful tool to infer the correction factors. Figure 21 shows the path of a single particle that scatters in the absorber module of the MICE experiment.

Each TOF provides a single space point in the global coordinate system. This position is assumed to be the true position with a large uncertainty due to the limited granularity of the detector. Trackers sample the particle track in five different stations and this allows for the reconstruction of a straight track without any assumption  
420 made on the prior position of the tracker. In global coordinates, on average, the track reconstructed between TOF1 and TOF2 should agree with the track reconstructed in either tracker, i.e. the mean residuals should be zero. Applying this reasoning to the unknown offset and angles yields to a system of equations for the four unknown constants [18]. The measurement of four residual distributions per tracker yields the alignment constants. The main source of bias is the scattering in the material between TOF1 and TOF2. If the beam is not  
425 perfectly centred, particles preferentially scrape out on one side of the magnet bore, anisotropically curbing a specific tail of the residual distribution. To nullify this effect, a fiducial cut is applied to the upstream sample. Only particles that are expected to be contained in the downstream tracker are included in the analysis.

Data is recorded with the superconducting magnetic channel of the experiment turned off, i.e. with tracks going in a straight line from TOF1 to the beam dump. High momentum beams are used in order to reduce  
430 the RMS scattering angle and maximize transmission. Each data set was processed independently with the algorithm. Figure 22 compiles the alignment parameters measured for each run during a specific ISIS user cycle. The measurements are in good agreement with one another and show no significant discrepancy: an

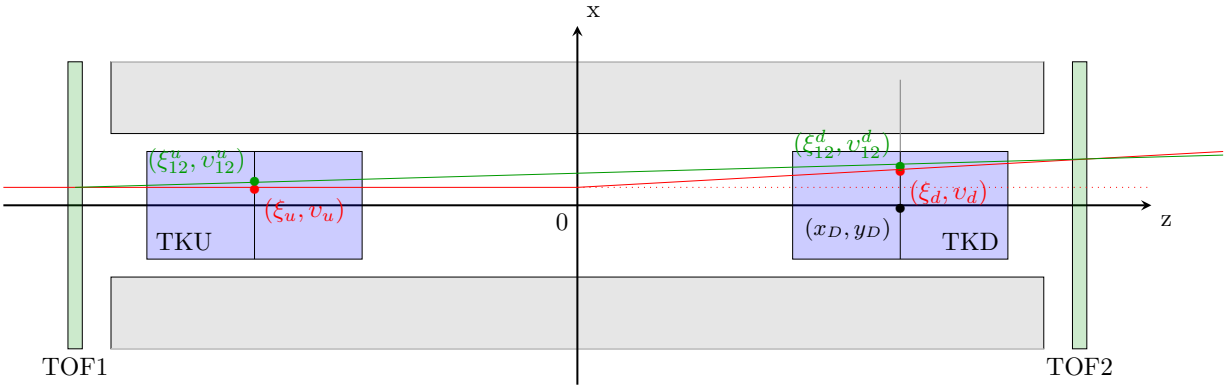


Figure 21: True path of a single particle track (red) and its path as reconstructed from the time-of-flight system (green). The position of the track at the tracker centres is represented by markers.

agreement between the independent fits guarantees an unbiased measurement of the alignment constants. The constant fit  $\chi^2/\text{ndf}$  is close to unity for each fit, which indicates that there are no significant additional source of uncertainty. The optimal parameters are summarised in table 7.

	x [mm]	y [mm]	$\alpha$ [mrad]	$\beta$ [mrad]
TKU	$-0.032 \pm 0.094$	$-1.538 \pm 0.095$	$3.382 \pm 0.030$	$0.412 \pm 0.029$
TKD	$-2.958 \pm 0.095$	$2.921 \pm 0.096$	$-0.036 \pm 0.030$	$1.333 \pm 0.030$

Table 7: Summary table of the optimal alignment constants measured in the high-momentum straight-track data acquired during the 2017/01 ISIS user cycle.

## 9 Liquid Hydrogen absorber

### 9.1 Introduction

As a muon beam passes through material, some of the kinetic energy of the muons is lost through ionization of the material. This process results in a reduction of the normalised transverse emittance and the beam is said to be cooled. Muons will also undergo multiple Coulomb scattering which increases the divergence of the beam, thereby increasing the normalised transverse emittance and heating the beam.

The absorber vessel comprised a cylindrical aluminium body sealed with two thin aluminium end windows, as shown in the right panel of figure 23. The absorber vessel was specified to contain 22 l of liquid, so the body had an inner diameter of 300 mm and a length between its end flanges of 230 mm. The length along the central axis between the two domes of the thin aluminium end windows was 350 mm [19].

The following sections detail the important effects that could contribute to the systematic error of the measured energy loss and scattering in the absorber and thus the cooling effect.

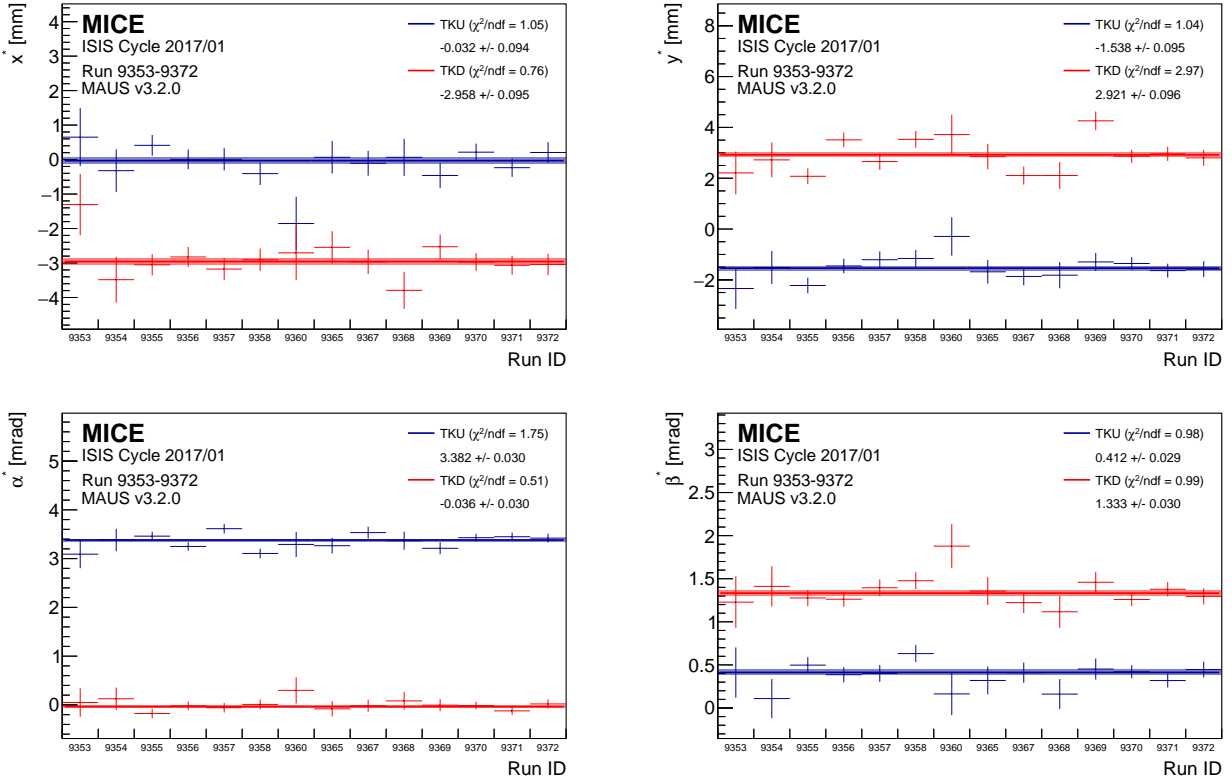


Figure 22: Consistency of the alignment algorithm across runs acquired during the 2017/01 ISIS user cycle.

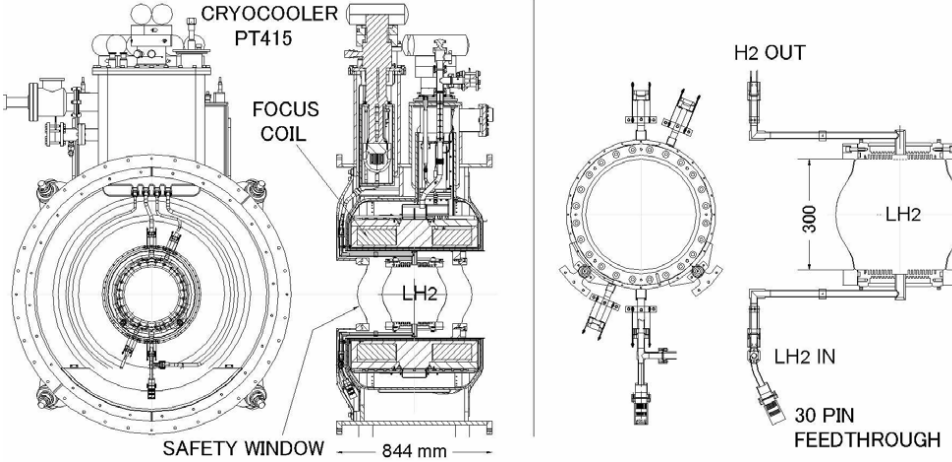


Figure 23: Left panel: Drawing of the absorber/focus-coil (AFC) module showing the principal components. Right panel: detail of the liquid-hydrogen absorber vessel.

## 9.2 Systematic studies

### 9.2.1 Variation of the density of liquid Hydrogen due to varying temperature and pressure

450 The energy lost by a muon travelling through the liquid Hydrogen absorber depends on the path length the muon travelled through and on the density of the liquid Hydrogen. The density of liquid Hydrogen changes at

different temperatures and pressures. To know how much energy the muon lost, we need to accurately know the temperature and pressure to determine the density.

The temperature was recorded by eight LakeShore Cernox 1050 SD sensors with a resolution of 0.1 K. Four of the sensors were used solely as temperature sensors, while the other four were used also as level sensors to ensure the liquid Hydrogen reached the top of the vessel. They were arranged in pairs with two mechanically clamped at the top of the vessel, two at a rotation of 45°, a further two at a further rotation of 90° and a final two at a further rotation of 45° to be at the bottom of the vessel.

Coldown and liquefaction were completed slowly over eight days until the 25 September 2017 at a pressure of 1.15 Bar after which the vessel's pressure was lowered to 1.085 Bar and stabilised during the early hours of the 26 September 2017 [19]. The vessel then remained in this steady-state equilibrium until the 16 October 2017 when the venting process began. During this process the coldhead was switched off and the heaters were switched on, delivering a nominal power of 50 Watt to the absorber vessel. This resulted in an increase in pressure and temperature until it stabilised at the boiling temperature. At this temperature the liquid Hydrogen turned to gas and began emptying from the vessel. A rapid increase in temperature followed once all the liquid Hydrogen had boiled off.

The sensors have a typical accuracy of  $\pm 9\text{mK}$  and a long-term stability of  $\pm 12\text{mK}$  at 20K. The magnetic field dependent temperature error at 2.5T is 0.04%  $\Delta T/T$ , equivalent to  $\pm 8\text{mK}$  at 20K [20][21]. These are the quoted uncertainties given by the manufacturer of the sensors. The importance of magnetic fields on temperature measurements is that they cause reversible calibration shifts: when the magnetic field is removed, the sensors return to their original calibration.

To reduce the uncertainty in the liquid Hydrogen density a calibration procedure was devised using the boiling point: the corrected temperature reading is found by applying a cut-off correction, a magnetic field correction based on the focus coil current and mode, and then a boiling point scaling factor [22].

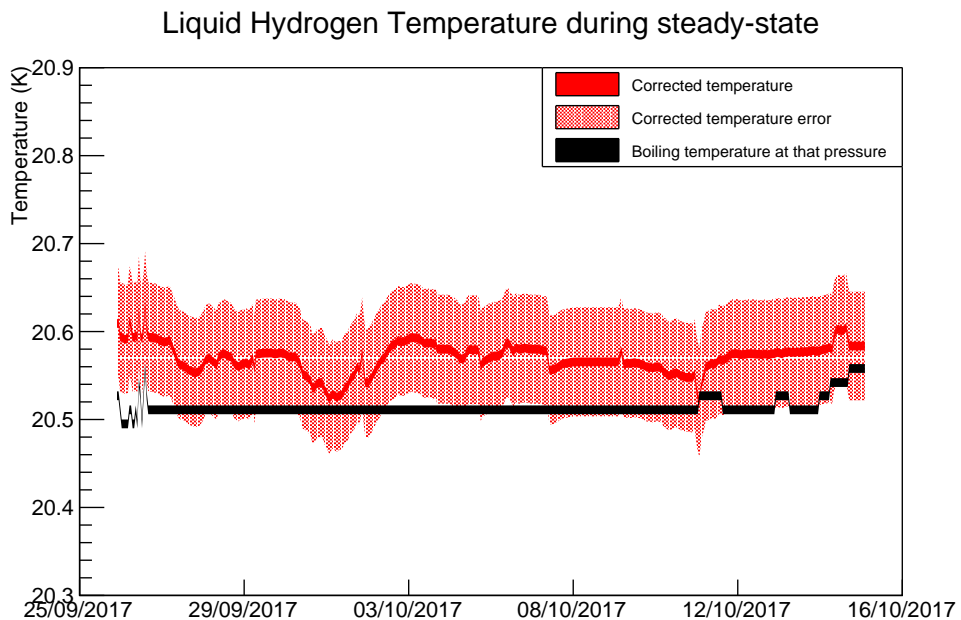


Figure 24: Temperature of the LH<sub>2</sub> during the steady-state period. After applying all the correction factors the sensors agree to within 0.2K of each other. During the steady-state the boiling point temperature is 20.511K.

The boiling temperature at 1.085 Bar is 20.511K, with our corrected sensor readings slightly higher (Fig. 24). There are however a number of uncertainties. The sensors add another 29mK (9mK accuracy + 12mK

stability + 8mK magnetic field), although the magnetic field error is likely greater. The temperature scaling and magnet current correction factors also have an associated error as they are based on the 0.1K resolution. The pressure uncertainty ( $\pm 5\text{mBar}$ ) adds another uncertainty to the temperature calibration constants of  $\pm 0.014\text{K}$ .  
480 Collectively, all these uncertainties add up to 0.2K.

Knowing that in our steady state condition the liquid Hydrogen was close to the boiling temperature of liquid Parahydrogen [22] at  $20.5\text{K} \pm 0.2\text{K}$  and 1.085 Bar allows us to determine the uncertainty in the density as  $70.54\text{kg/m}^3 \pm 0.24\text{kg/m}^3$

### 9.2.2 Contraction of the absorber vessel due to cooling

485 The Aluminium absorber vessel was cooled from room temperature to the operating temperature of the experiment ( $\approx 20.3\text{K}$ ), which resulted in the vessel contracting. The linear contraction of Al-6061 as it is cooled from 293K is given by the equation

$$\alpha = -4.1277 \times 10^{-3}T - 3.0389 \times 10^{-6}T^2 + 8.7696 \times 10^{-8}T^3 - 9.9821 \times 10^{-11}T^4 \quad (5)$$

where T is the operating temperature [23]. The equation is a line of best fit of data collated by NIST (National Institute of Standards and Technology) and has an associated curve fit error of 4%.

490 At the MICE operating temperature, this corresponds to a linear contraction of the vessel along each plane of 0.415% ( $293\text{K} \rightarrow 20.3\text{K}$ ), resulting in a warm bore length (350mm) contraction of 1.4525mm  $\pm 4\%$ . The vessel was held suspended in place, meaning the vessel was free to contract along each plane without restriction, ensuring there were no forces created to distort the shape of the vessel.

### 9.2.3 Deflection of absorber vessel windows due to internal pressure

495 To minimise energy loss and Coulomb scattering by the absorber vessel, the windows were kept as thin as possible. They must however not rupture when handling any internal pressure they are subjected to. For safety considerations [19][24] it is necessary for the liquid hydrogen circuit to be pressurised above atmospheric pressure to prevent air ingress. The vessel must also be capable of handling up to 1.5 Bar, the relief valve set pressure.

500 These pressures resulted in a deflection of the absorber windows and were modelled using ANSYS [25]. The uncertainty in the model's window deflection was 20%. It showed a linear expansion of the window deflection with pressure up to 2 Bar when the windows begin to yield.

The pressure sensors are accurate to  $\pm 5\text{mBar}$  (0.25% of 2 BarA Full Scale). At  $1085 \pm 5\text{ mBar}$ , the typical MICE operating pressure, this corresponds to a deflection of  $0.5374\text{mm} \pm 0.1076\text{mm}$  (model uncertainty)  $\pm 0.0022\text{mm}$  (sensor uncertainty) at the centre of the absorber window.  
505

### 9.2.4 Variation of the absorber vessel window thicknesses

The amount of energy loss and cooling experienced by a muon passing through the absorber depends on the amount of Aluminium and liquid Hydrogen traversed. There are four windows, two absorber wall windows of the vessel and two safety windows.

510 At the centre of the absorber, the total amount of Aluminium the muon beam passes through is  $785 \pm 24$  microns, a variance of 3.057%. However, as the windows are thin, the effects on energy loss are negligible. A 200MeV muon passing along the central axis of an empty absorber loses 0.345 MeV, which introduces a 0.01 MeV uncertainty on energy loss.

## 9.2.5 Total Systematic Uncertainty on Energy Loss

515 In total there are three main contributions to the systematic uncertainty of the liquid Hydrogen absorber on energy loss. The contraction of the absorber and deflection of the absorber window due to internal pressure (Eq. 6) reduces the central warm bore length by  $0.4 \pm 0.3\text{mm}$ .

$$1.4525 (\pm 0.0581) - 2(0.5374 (\pm 0.1098)) = 0.3777 \pm 0.2777 = 0.4\text{mm} \pm 0.3\text{mm} \quad (6)$$

520 The combined absorber window thickness variation at the centre of the absorber is 24 microns. The temperature during the steady state period of the experiment when the pressure remained constant at  $1085 \pm 5\text{ mBar}$  is  $20.5 \pm 0.2\text{K}$  corresponding to a liquid Hydrogen density of  $70.54 \pm 0.24\text{kg/m}^3$ .

The energy loss is momentum dependent as each particle will lose a different amount of energy passing through the absorber. Tables 8 and 9 show the energy loss at various momenta and densities of Aluminium and liquid Hydrogen [26][27][28][29]. 277 MeV and 344 MeV are the minimum ionization momenta of Aluminium and liquid Hydrogen respectively.

Table 8: Energy Loss for Aluminium (Al-6061) at various momenta with a density of  $2.699\text{ g/cm}^3$ .

Momentum (MeV)	100	140	200	277
Mass Stopping Power ( $\text{MeVg}^{-1}\text{cm}^2$ )	1.798	1.688	1.630	1.615
Stopping Power ( $\text{MeVcm}^{-1}$ )	4.8528	4.556	4.3994	4.3589

525 During the MICE experiment 140, 170, 200 and 240 MeV momenta muon beams were used. The energy loss and its uncertainty were then be calculated. The calculation used a central bore length of  $349.6 \pm 0.3\text{mm}$ , a total window thickness of  $0.785 \pm 0.024\text{mm}$  and a liquid Hydrogen density of  $70.54 \pm 0.24\text{kg/m}^3$  for a particle travelling straight through the centre of the absorber.

530 For a 140 MeV muon particle this corresponds to an energy loss of  $10.88 \pm 0.06 (\pm 0.51\%) \text{ MeV}$ , while for a 200 MeV muon particle this corresponds to an energy loss of  $10.44 \pm 0.05 (\pm 0.51\%) \text{ MeV}$ . In terms of Energy loss, the systematic error is 0.51%. This is for a particle travelling along the central axis of the absorber. An actual muon travelling through the absorber with a magnetic field will take a different path and thus have a different path length of Aluminium and liquid Hydrogen traversed.

Table 9: Energy loss for liquid Hydrogen at various densities ( $0.0703$  to  $0.0708\text{ g/cm}^3$ ) and various momenta of muons.

Momentum	100	140	200	344
Mass Stopping Power	4.568	4.267	4.104	4.034
Stopping Power (at $\rho=0.0703$ )	0.3211	0.29997	0.2885	0.28359
Stopping Power (at $\rho=0.07054$ )	0.3222	0.30099	0.2895	0.2846
Stopping Power (at $\rho=0.07078$ )	0.3233	0.3020	0.29048	0.2855
Stopping Power (at $\rho=0.0708$ )	0.3234	0.3021	0.29056	0.2856

## **10 Conclusions**

535 To be written at last.

## References

- [1] M. Bonesini, “The design of MICE TOF0 detector,” *MICE Note 145* (2006) .  
<http://mice.iit.edu/micenotes/public/pdf/MICE0145/MICE0145.pdf>.
- [2] R. Bertoni *et al.*, “The construction and laboratory tests for MICE TOF0/1 detectors,” *MICE Note 241* (2008) . <http://mice.iit.edu/micenotes/public/pdf/MICE0241/MICE0241.pdf>.
- [3] R. Bertoni, A. Blondel, M. Bonesini, G. Cecchet, A. de Bari, J. S. Graulich, Y. Karadzhov, M. Rayner, I. Rusinov, R. Tsenev, S. Terzo, and V. Verguilov, “The design and commissioning of the MICE upstream time-of-flight system,” *Nuclear Instruments and Methods in Physics Research A* **615** (Mar., 2010) 14–26, arXiv:1001.4426 [physics.ins-det].
- [4] R. Bertoni *et al.*, “The construction of the MICE TOF2 detector,” *MICE Note 286* (2010) .  
<http://mice.iit.edu/micenotes/public/pdf/MICE0286/MICE0286.pdf>.
- [5] D. Rajaram and V. C. Palladino, “The Status of MICE Step IV,”.  
<http://accelconf.web.cern.ch/AccelConf/IPAC2015/papers/thpf122.pdf>.
- [6] M. Bonesini, “Progress of the MICE experiment,” arXiv:1510.08825 [physics.acc-ph].
- [7] The MICE Collaboration, “Characterisation of the muon beams for the Muon Ionisation Cooling Experiment,” *ArXiv e-prints* (June, 2013) , arXiv:1306.1509 [physics.acc-ph].
- [8] D. Adams *et al.*, “Pion contamination in the MICE muon beam,” *Journal of Instrumentation* **11** (Mar., 2016) P03001, arXiv:1511.00556 [physics.ins-det].
- [9] M. A. Rayner, *The development of a novel technique for characterizing the MICE muon beam and demonstrating its suitability for a muon cooling measurement*. PhD thesis, Oxford U., 2011.  
<http://lss.fnal.gov/archive/other/thesis/rayner-m.pdf>.
- [10] Y. Karadzhov *et al.*, “TOF detectors Time Calibration,” *MICE Note 251* (2009) .  
<http://mice.iit.edu/micenotes/public/pdf/MICE0251/MICE0251.pdf>.
- [11] L. Cremaldi *et al.*, “Progress on Cherenkov Reconstruction in MICE,” *MICE Note 473* (2015) .  
<http://mice.iit.edu/micenotes/public/pdf/MICE0473/MICE0473.pdf>.
- [12] R. Asfandiyarov *et al.*, “The design and construction of the MICE Electron-Muon Ranger,” *Journal of Instrumentation* **11** (Oct., 2016) T10007, arXiv:1607.04955 [physics.ins-det].
- [13] F. Drielsma, “Electron-Muon Ranger: hardware characterization,” Master’s thesis, University of Geneva, 2014. <https://arxiv.org/abs/1710.06946>.
- [14] D. Adams *et al.*, “Electron-muon ranger: performance in the MICE muon beam,” *Journal of Instrumentation* **10** (Dec., 2015) P12012, arXiv:1510.08306 [physics.ins-det].
- [15] F. Drielsma, *Measurement of the Increase in Phase Space Density of a Muon Beam through Ionization Cooling*. PhD thesis, University of Geneva, 10, 2018.
- [16] M. Ellis *et al.*, “The Design, construction and performance of the MICE scintillating fibre trackers,” *Nucl. Instrum. Meth.* **A659** (2011) 136–153, 1005.3491.
- [17] **D0** Collaboration, V. M. Abazov *et al.*, “The Upgraded D0 detector,” *Nucl. Instrum. Meth.* **A565** (2006) 463–537, physics/0507191.

- [18] F. Drielsma, “Beam-based detector alignment in the MICE muon beam line,” arXiv:1805.06623 [physics.ins-det]. <https://arxiv.org/abs/1805.06623>.
- 575 [19] V. Bayliss *et al.*, “The liquid-hydrogen absorber for mice,” *Journal of Instrumentation* **13** no. 09, (2018) T09008. <http://stacks.iop.org/1748-0221/13/i=09/a=T09008>.
- [20] “Cernox RTDs [Accessed 2 Oct. 2018],”.  
[https://www.lakeshore.com/Documents/LSTC\\_Cernox\\_1.pdf](https://www.lakeshore.com/Documents/LSTC_Cernox_1.pdf).
- 580 [21] “Temperature Measurement and Control Catalog [Accessed 2 Oct. 2018],”.  
[https://www.lakeshore.com/Documents/LakeShoreTC\\_1.pdf](https://www.lakeshore.com/Documents/LakeShoreTC_1.pdf).
- [22] C. Brown *et al.*, “Systematic Uncertainties in the LH2 absorber,” *MICE Note 524* (2018) .  
<http://mice.iit.edu/micenotes/public/pdf/MICE0524/MICE0524.pdf>.
- [23] G. Hardin, “Aluminum 6061-T6 (UNS AA96061) [Accessed 3 Oct. 2018],”.  
<https://www.nist.gov/mml/acmd/aluminum-6061-t6-uns-aa96061>.
- 585 [24] S. Ishimoto *et al.*, “Liquid Hydrogen Absorber for MICE,” *Conf. Proc. C100523* (2010) 421–423.
- [25] M. Green *et al.*, “Does One Know the Properties of a MICE Solid or Liquid Absorber to Better than 0.3 Percent?,” *MICE Note 155* (2006) .  
<http://mice.iit.edu/micenotes/public/pdf/MICE0155/MICE0155.pdf>.
- [26] “Atomic and nuclear properties of Aluminium,”.  
[http://pdg.lbl.gov/2017/AtomicNuclearProperties/HTML/aluminum\\_Al.html](http://pdg.lbl.gov/2017/AtomicNuclearProperties/HTML/aluminum_Al.html).
- 590 [27] “Atomic and nuclear properties of liquid Hydrogen,”. [http://pdg.lbl.gov/2017/AtomicNuclearProperties/HTML/liquid\\_hydrogen.html](http://pdg.lbl.gov/2017/AtomicNuclearProperties/HTML/liquid_hydrogen.html).
- [28] “Muon in Aluminium,”. [http://pdg.lbl.gov/2017/AtomicNuclearProperties/MUE/muE\\_aluminum\\_Al.pdf](http://pdg.lbl.gov/2017/AtomicNuclearProperties/MUE/muE_aluminum_Al.pdf).
- 595 [29] “Muons in liquid Hydrogen,”. [http://pdg.lbl.gov/2017/AtomicNuclearProperties/MUE/muE\\_liquid\\_hydrogen.pdf](http://pdg.lbl.gov/2017/AtomicNuclearProperties/MUE/muE_liquid_hydrogen.pdf).